Nano Energy 57 (2019) 230–240

Contents lists available at ScienceDirect

Nano Energy

journal homepage: www.elsevier.com/locate/nanoen

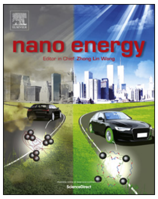

Full paper

Designing a highly efficient polysulfide conversion catalyst with paramontroseite for high-performance and long-life lithium-sulfur batteries

Sizhe Wang[a,b], Jiaxuan Liao[b], Xiaofei Yang[a], Jianneng Liang[a], Qian Sun[a], Jianwen Liang[a], Feipeng Zhao[a], Alicia Koo[a], Fanpeng Kong[a], Yao Yao[a], Xuejie Gao[a], Mengqiang Wu[b,*], Shi-Ze Yang[c,*], Ruying Li[a], Xueliang Sun[a,*]

[a] *Department of Mechanical and Materials Engineering, University of Western Ontario, London, Ontario, Canada N6A 5B9*
[b] *School of materials and energy, University of Electronic Science and Technology of China, Chengdu 611731, PR China*
[c] *Materials Science and Technology Division, Oak Ridge National Laboratory, Oak Ridge, TN 37831, USA*

ARTICLE INFO

Keywords:
Free-standing
Paramontroseite
Carbon nanotube
Catalyst
Lithium sulfur battery

ABSTRACT

Numerous efforts have been made to design the cathode of Li–S batteries to enhance reversible capacity and long-term cycling stability. However, challenges remain in achieving high electronic/ionic conductivity and suppressing the shuttle effect, especially for cathodes with high sulfur loading. Here we report a 3D free-standing hierarchical structure of VO_2(P) (paramontroseite VO_2) nanoparticles grown on nitrogen-doped carbon nanotube (NCNT) arrays as a catalytic host for high-performance sulfur cathodes. In this architecture, the VO_2(P) nanoparticles function as catalysts to oxidize the LiPS to produce thiosulfate due to the strong chemical interaction. Furthermore, thiosulfates act as a mediator to catenate long-chain LiPS together and convert short-chain Li_2S_2/Li_2S and surface-bound polythionate complexes. Accordingly, the VO_2(P)-NCNT/S cathode exhibits excellent performance with high discharge capacity output (≈1200 mA h g^{-1} at 0.2 C), stable long-term cycling (≈67% retention at 2 C for 500 cycles), and high sulfur loading cycling (initial areal capacity of 10.2 mA h cm^{-2} at 0.2 C for 200 cycles). This nanostructure catalytic cathode with high sulfur loadings, as well as stable cycling performances, is attractive for developing practically useable Li-S batteries.

1. Introduction

The lithium-sulfur (Li-S) battery is one of the most promising alternatives to the prevailing conventional lithium-ion batteries (LIBs) to meet the ever-increasing demands for high energy density, low cost, and high safety of energy storage systems [1,2]. Li–S batteries could supply a high theoretical capacity of 1675 mA h g^{-1} (10 times higher than that of LIBs) and a high theoretical energy density of 2567 kW kg^{-1} (5 times higher than that of LIBs). Meanwhile, elemental sulfur is nontoxic and widely accessible at a low cost which is essential for meeting energy conservation and sustainable development standards. However, the practical application of state-of-the-art Li–S batteries is still hindered by significant challenges such as low sulfur utilization, poor Coulombic efficiency, fast capacity degradation, severe self-discharge, and short cycle life due to the intrinsically low electronic conductivity of sulfur and lithium polysulfide (LiPS) shuttle reactions [3,4].

Different carbon materials have been reported as the host to as hosts to immobilize sulfur [1,5–8]. However, normal carbon materials always have a nonpolar surface, which is hardly to trap and restrict LiPS shuttle reactions. In contrast, nanostructured inorganic compounds have a strong chemical affinity with LiPS and prevent the diffusion of LiPS more effectively than carbon materials [9]. Even so, both these materials depend on physical or chemical adsorption to prevent LiPS shuttling and are merely palliative solutions which do not address the fundamental problems.

An alternative strategy to suppress the shuttle effect is to convert LiPS into insoluble Li_2S_2/Li_2S to minimize their dissolution and diffusion into the electrolyte [7]. Recent studies have shown that many polar hosts, such as metal oxides [10–16], metal sulfides [17–21], metal nitrides [22–24], metal carbide [25], and some metal-free materials [26–31] not only have a strong affinity to LiPS but also catalytically promote the conversion of LiPS to solid Li_2S_2/Li_2S. Nazar et al. proposed a way to entrap LiPS in the cathode relies on MnO_2 nanosheets binding and reacting with higher-order LiPS to convert them on reduction to insoluble lithium sulfide via disproportionation [11].

---

* Corresponding authors.
E-mail addresses: mwu@uestc.edu.cn (M. Wu), yangs1@ornl.gov (S.-Z. Yang), xsun@eng.uwo.ca (X. Sun).

https://doi.org/10.1016/j.nanoen.2018.12.020
Received 28 October 2018; Received in revised form 5 December 2018; Accepted 8 December 2018

Zhang et al. utilized the interface between CoS_2 and the electrolyte, which served as strong adsorption and activation sites for polar polysulfides to accelerate redox reactions of LiPS [17]. Lee et al. demonstrated the effectiveness of $MoS_{2\text{-}x}$/rGO as a catalyst for LiPS conversion in a sulfur cathode, in which the surface sulfur deficiencies participated in the LiPS conversion and improved the kinetics of LiPS redox reactions [18]. Yang et al. reported a twinborn TiO_2-TiN heterostructure electrode that achieves a smooth trapping-diffusion-conversion of LiPS across the interface [22].

Vanadium dioxides with a series of different polymorphs such as VO_2(A), VO_2(B), VO_2(C), VO_2(R), and VO_2(M) and mineral phases such as paramontroseite and nsutite-type VO_2 have received great interest in device applications owing to its unique metal-insulator transition with abundant structural phases, low cost, and controllable morphologies [32–34]. Nazar et al. report a metastable VO_2(B) with high chemical reactivity to anchor LiPS, which has a redox potential that lies just above the typical redox potential range (> 2.4 V) of soluble LiPS [35]. Fan et al. construct a VO_2(B)-VN binary host, accomplishing smooth immobilization-diffusion-conversion of LiPS to improve the electrochemical performance of Li–S batteries [36]. However, the VO_2(B) is metastable and tends to transition into the VO_2(A) phase under 160 °C and VO_2(M) under 300 °C [37,38]. Moreover, VO_2(B) shows semiconductor characteristics with low intrinsic electrical conductivity [39], which will hinder the catalytic conversion of LiPS by VO_2(B) [36].

Paramontroseite vanadium dioxide (VO_2(P)), a minor structure, was first discovered in minerals during the 1950s [40]. The VO_2(P) is composed of infinite chains along the c-axis with nearest V–V distances of 0.293 nm, in which d-orbital electrons would be shared by all of the metal V atoms along the c-axis in paramontroseite similar to that in metallic rutile VO_2(R) [32]. Among the family of VO_2, the VO_2(P) was revealed to have the most promising electrical conducting properties at room temperature from the structural and its calculation results. However, few references have reported its application in energy storage devices due to the hindered synthetic route [41]. To the best of our knowledge, our work is the first to introduce VO_2(P) into a Li-S battery host.

Herein, we present NCNTs vertically grown on carbon paper as a free-standing carbon-based host onto which the VO_2(P) nanoparticles and sulfur are uniformly deposited for use as a cathode material, henceforth abbreviated as the VO_2(P)-NCNT host. The 3D structure with vertically aligned NCNTs have a high surface area and enable uniform distribution of sulfur for high sulfur loading while also facilitating the electron/ion transport between the sulfur and host to improve cathode conductivity. In addition, VO_2(P) nanoparticles are also uniformly distributed and could effectively enhance the charge transfer and redox reaction kinetics as a catalytic mediator. This VO_2(P)-NCNT/S cathode has stable long-term cycling life (over 500 cycles with 67% retention) under a high rate of 2 C. This cathode with high sulfur loading (up to 9.6 mg cm^{-2}) also demonstrates its superior performance. Furthermore, the mechanisms of enhancing redox kinetics and catalysis of LiPS conversion with VO_2(P) are also discussed.

2. Experimental section

2.1. Preparation of free-standing NCNT host

The NCNT free-standing cathode was prepared by using a spray pyrolysis chemical vapor deposition (SPCVD) method, as described previously [42]. A piece of carbon paper (CP) was sputtered with aluminum as the buffer layer. The CP was then fixed inside a vertical quartz tube of a chemical vapor deposition furnace. The furnace was heated up to 850 °C in 20 min under Ar with the flow rate of 240 sccm. After the temperature reached 850 °C, a catalytic solution A (1 g ferrocene in 50 mL acetonitrile) was introduced into the tube under an ultrasonic probe sonicator at a flow rate of 250 μL/min for 6 min. Then, a solution B (10 g imidazole in 50 mL acetonitrile) was introduced into the tube under the same condition for ~35 min. After the SPCVD process, the NCNT arrays were grown vertically on the surface of the CP.

2.2. Preparation of free-standing VO_2(P)-NCNT host

The VO_2(P)-NCNT host was prepared by using a facile hydrothermal method, as described elsewhere [39]. In a typical synthesis, 1.6 mmol Na_3VO_4 and 8 mmol thioacetamide (TAA) were dissolved in 40 mL distilled water with continuous stirring to form a homogeneous solution. And then 4 mmol NH_4F was also added into the as-obtained solution to adjust the pH. Then this solution was transferred into a 50 mL Teflon-lined autoclave together with the free-standing NCNT-CP, which was sealed and heated at 180 °C for 20 h. After the hydrothermal process, the VO_2(P)-NCNT free-standing cathode was alternately washed with ethanol and distilled water 3 times, and finally dried in an 120 °C vacuum oven. To control the morphology of the VO_2(P) nanoparticles, VO_2(P)-NCNT cathodes with different contents of precursors (0.6, 1.1, and 2.1 mmol Na_3VO_4; 3, 5.5, 10.5 mmol TAA) are also prepared.

2.3. Preparation of VO_2(P)-NCNT/S cathode

The sulfur active material was introduced into the free-standing hosts by controlled drop casting sulfur solution in CS_2 (100 mg sulfur in 5 mL CS_2), giving sulfur cathodes of VO_2(P)-NCNT/S and NCNT/S. To uniformly distribute sulfur in the VO_2(P)-NCNT/S cathode, the same process was repeated several times. Finally, the VO_2(P)-NCNT/S cathodes were dried in a vacuum oven at 60 °C for 6 h. The regular sulfur loading is about 2.0 mg cm^{-2}. The cathodes with high areal sulfur loadings of 6.4 and 9.6 mg cm^{-2} were also prepared to test the stability of cycling performances.

2.4. Adsorption properties of lithium polysulfides

Li_2S_4 and Li_2S_6 solutions were prepared by mixing Li_2S and S with a molar ratio of 1:3 and 1:5, respectively, into a 1:1 (v/v) DOL/DME mixture, and stirred overnight at 60 °C. 4 mg of NCNT or VO_2(P)-NCNT powder was exfoliated from the hosts and added into 2 mL of a 4 mmol L^{-1} Li_2S_4 stock solution. Similarly, 6 mg of NCNT or VO_2(P)-NCNT powder were added into 3 mL of a 5 mmol L^{-1} Li_2S_6 stock solution. The mixtures were stirred to facilitate adsorptions.

2.5. Preparation of VO_2(P)-NCNT@Li_2S_4

In an Ar-filled glovebox, a piece of VO_2(P)-NCNT host was soaked in a solution containing 1 mmol Li_2S_4 in 5 mL dimethyl ether (DME) for 12 h. The host was then washed and dried in a glovebox.

2.6. Materials characterization

The morphologies were characterized using scanning electronic microscopy (FESEM, Hitachi S-4800) and scanning transmission electron microscopy (STEM, FEI Talos F200X). X-ray photoelectron spectroscopy (XPS, ESCALAB 250Xi) with focused monochromatized Al Kα radiation (1486.6 eV) was used to analyze the elemental composition and valence state. X-ray diffraction (XRD, Bruker D8 advanced) with Cu Kα radiation (λ = 1.5415 Å) and Raman spectroscopy (HORIBA Scientific LabRAM) with 632.8 nm HeNe laser were used to analyze the structure, composition and chemical bonds of these samples. The nitrogen sorption isotherm was recorded on a gas sorptometer (Micromeritics 3Flex 3500). Thermogravimetric analysis (TGA, TA SDT Q600) was performed in air at a heating rate of 5 °C min^{-1}. X-ray absorption near edge structure (XANES) spectra of sulfur K-edge and vanadium K-edge were measured on the Soft X-ray Microcharacterization beamline (SXRMB) at the Canadian Light Source (CLS) in Saskatoon. To avoid the contamination of samples, all the samples were sealed using Kapton tape in an argon-filled glove box.

2.7. Symmetrical cell assembly and measurements

The electrodes for symmetrical cells were fabricated without the presence of elemental sulfur. VO_2(P)-NCNT disks were used as identical working and counter electrode with 60 μL electrolyte (0.5 mol L^{-1} Li_2S_6 and 1 mol L^{-1} LiTFSI dissolved in DOL/DME (v/v = 1/1)). Cyclic voltammetry (CV) measurements of the symmetrical cells were performed at a scan rate of 50 mV s^{-1} between − 1.0 V and 1.0 V.

2.8. Electrochemical characterization

Standard CR2032-type coin cells were assembled in an Ar-filled glove box with oxygen and moisture content below 1 ppm. The electrolyte was 1.0 M lithium bis(trifluoromethanesulfonyl)imide (LiTFSI) dissolved in mixed solvent of 1,3-dioxolane (DOL) and DME (v/v = 1:1) with 1 wt% of $LiNO_3$ as an additive. The amount of electrolyte used in a coin cell is about 80–120 μL. The galvanostatic charge/discharge tests and galvanostatic intermittent titration technique (GITT) of the cells were measured on a Land T2001A battery testing station with a voltage range of 1.7–2.8 V. Through a VMP3 electrochemical workstation, cyclic voltammetry (CV) was performed at a scan rate of 0.1 mV s^{-1} and electrochemical impedance spectroscopy (EIS) was tested with a frequency range of 100 kHz to 0.1 Hz.

3. Results and discussion

3.1. Materials characterization

The synthesis of the VO_2(P)-NCNT composite host is illustrated in Fig. 1a. The free-standing NCNT collector was prepared on carbon paper (CP) through a two-step method, as described elsewhere [42]. The CP substrate exhibits a 3D structure composed of randomly oriented carbon fibers with a diameter of ~10 μm (Fig. S1). A uniform layer of NCNTs of approximately 40 μm in length is grown on the CP, covering the carbon fibers (Fig. S2), followed by the deposition of uniform VO_2(P) nanoparticles with an average particle size of ~120 nm (Fig. 1b–d) via a facile hydrothermal method. The size and amount of the particles are controlled by the concentration of the precursors. The FESEM images of the four samples with increased precursor concentrations resulting in different morphologies are shown in Fig. S3. The free-standing and flexible features of this 3D structured VO_2(P)-NCNT host are also shown in Fig. S4. The elemental mapping images suggested the uniform concentration distributions in large scale (Fig. S5).

The TEM micrographs of NCNTs display their characteristic bamboo-like features with a stacked cone structure (Fig. 1e). The uniform growth of spherical VO_2(P) nanoparticles with a diameter of ~120 nm on NCNTs can also be observed (Fig. 1b-d.). The TEM images with selected-area electron diffraction (SAED) pattern were used to investigate the VO_2(P) nanoparticles grown on NCNT (Fig. 1f-g). The distances between adjacent lattice planes (d-spacing) were measured to be ~0.234 nm, corresponding to the (111) plane of orthorhombic phase of paramontroseite VO_2, which is in good agreement with the SAED pattern (Fig. 1h) [41]. Energy dispersive X-ray (EDS) mapping images (Fig. 1i–m) with the distributions of V, O, and C suggested an atomic concentration gradient of VO_2(P) on the surface of the NCNT arrays with high uniformity. Similarly, the EELS elemental mappings are consistent with this result (Fig. S6).

XRD, Raman, XPS, and TGA/DSC measurements were performed to determine the detailed phase and composition of the VO_2(P)-NCNT sample. Fig. 2a shows the XRD patterns of the pure NCNT and VO_2(P)-NCNT, where the broad diffraction peaks at 26.5° and 43.2° agree well with the (002) and (004) planes of graphitic carbon (JCPDS 75-1621). For VO_2(P)-NCNT, apart from the peaks of NCNT, all the main peaks correspond to the orthorhombic phase of VO_2(P) with a space group of *I*2/*c* (JCPDS 73-0514) [41]. The super-cell structure of orthorhombic VO_2(P) projected along different orientations are shown in Fig. 2b and Fig. S7. In Fig. 2c, the intense peaks that appear between 150 and 1200 cm^{-1} are indexed well within the fingerprint region of the paramontroseite minor (RRUFF database: R050391). The D-band and G-band at ~1310 and ~1590 cm^{-1}, derived from NCNT, represent defect-induced vibrations of disordered carbon and vibration of the sp^2 bonded carbon atoms, respectively [43,44]. The XPS spectra of V 2p and O 1s peaks for the sample are shown in Fig. 2d. The V 2p3/2 and V 2p1/2 peaks at 516.6 and 524.0 eV correspond to V^{4+} in paramontroseite, and the corresponding spin-orbit splitting energy is 7.4 eV [45]. The tiny peaks of V 2p at 515.3 and 522.8 eV may derived from the trace amount of V^{3+} in V_2O_3. The peaks at 531.3, 530.0 and 519 eV are assigned to the O-H, O^{2-} and X-ray satellite groups, respectively [46]. The TGA/DSC curves of pure NCNT, VO_2(P), VO_2(P)-NCNT samples are shown in Fig. 2e. A weight increase of ~8.1 wt% over 300–550 °C in VO_2(P) could be associated with the oxidation process from VO_2 to V_2O_5 [47]. There is an endothermic peak at ~670 °C, which may be due to the melting point of V_2O_5 [38]. For the pure NCNT, there is another exothermic process with a weight loss of ~75 wt % at 350–500 °C (peak at 462 °C), which derives from the burning of NCNT. The nitrogen adsorption/desorption isotherm of the NCNT (Fig. 2f) shows a mixed shape of type II (at medium pressures) and type IV (at higher pressures) [42]. The BET surface area and total pore volume of pure CP, pure NCNT, VO_2(P)-NCNT hosts were determined to be 0.3, 37.0 and 21.3 m^2 g^{-1}, respectively. It should be noted that the BET surface area of VO_2(P)-NCNT exhibit more than 70 times than that of pure CP, thus could provide a much larger surface area to load much higher sulfur weight per unit area.

3.2. Electrochemical performance

Standard CR2032-type coin cells with Li metal as a counter electrode were assembled to measure the electrochemical performance of the VO_2(P)-NCNT/S cathode. In Fig. 3a, the cycling performances of VO_2(P)-NCNT/S and NCNT/S were examined at a current density of 0.2C (1C = 1672 mAh^{-1}). For the VO_2(P)-NCNT/S cathode, it delivers a stable cycling performance with a high reversible discharge capacity of ~1200 mAh g^{-1}. The capacity retention is above 94% after 100 cycles (compared to the 2nd cycle). For the pure NCNT/S cathode, the discharge capacity fades gradually and the capacity retention is only 63.3% after 100 cycles (compared to the 2nd cycle). To further compare the electrochemical performances, the rate capabilities of the VO_2(P)-NCNT/S and NCNT/S cathodes were measured under a stepwise current density program from 0.1 C to 2 C (Fig. 3b). The corresponding galvanostatic charge/discharge tests were shown in Fig. S8. The average reversible capacities of NCNT/S are 1030, 790, 765, 775, 680, 603, and 395 mA h g^{-1} at rates of 0.1, 0.2, 0.4, 0.6, 0.8, 1 and 2 C, respectively. However, the VO_2(P)-NCNT/S cathode shows significant high-rate improvement, with average reversible capacities of 1100, 982, 910, 886, 875, 864, and 760 mA h g^{-1} at rates of 0.1, 0.2, 0.4, 0.6, 0.8, 1 and 2 C, respectively, which is stable at the same current density. When the current density is returned to 0.2 C, the capacity can recover to a similar value of the initial step at 0.2 C. The better rate performance of VO_2(P)-NCNT/S indicates that the VO_2(P) nanoparticles play a key role in improving the rate performances due to the high conductivity in the composite host.

The cycling stability of the VO_2(P)-NCNT/S cathode was also investigated at 2 C for 500 cycles in Fig. 3c. The cathode maintains stable cycling performance with a reversible discharge capacity of ~880 mA h g^{-1}, which corresponds to a capacity retention of ~67% from the 2nd cycle. Even after 500 cycles, the cathode still delivers a high reversible discharge capacity of 780 mA h g^{-1}, while the capacity of NCNT/S cathode fades to 280 mA h g^{-1} after only 260 cycles (retaining 28.8% of its capacity of the 2th cycle). The higher reversible capacity and capacity retention of the VO_2(P)-NCNT/S cathode confirm the important role of the VO_2(P) in this 3D architecture. Figs. S9 and

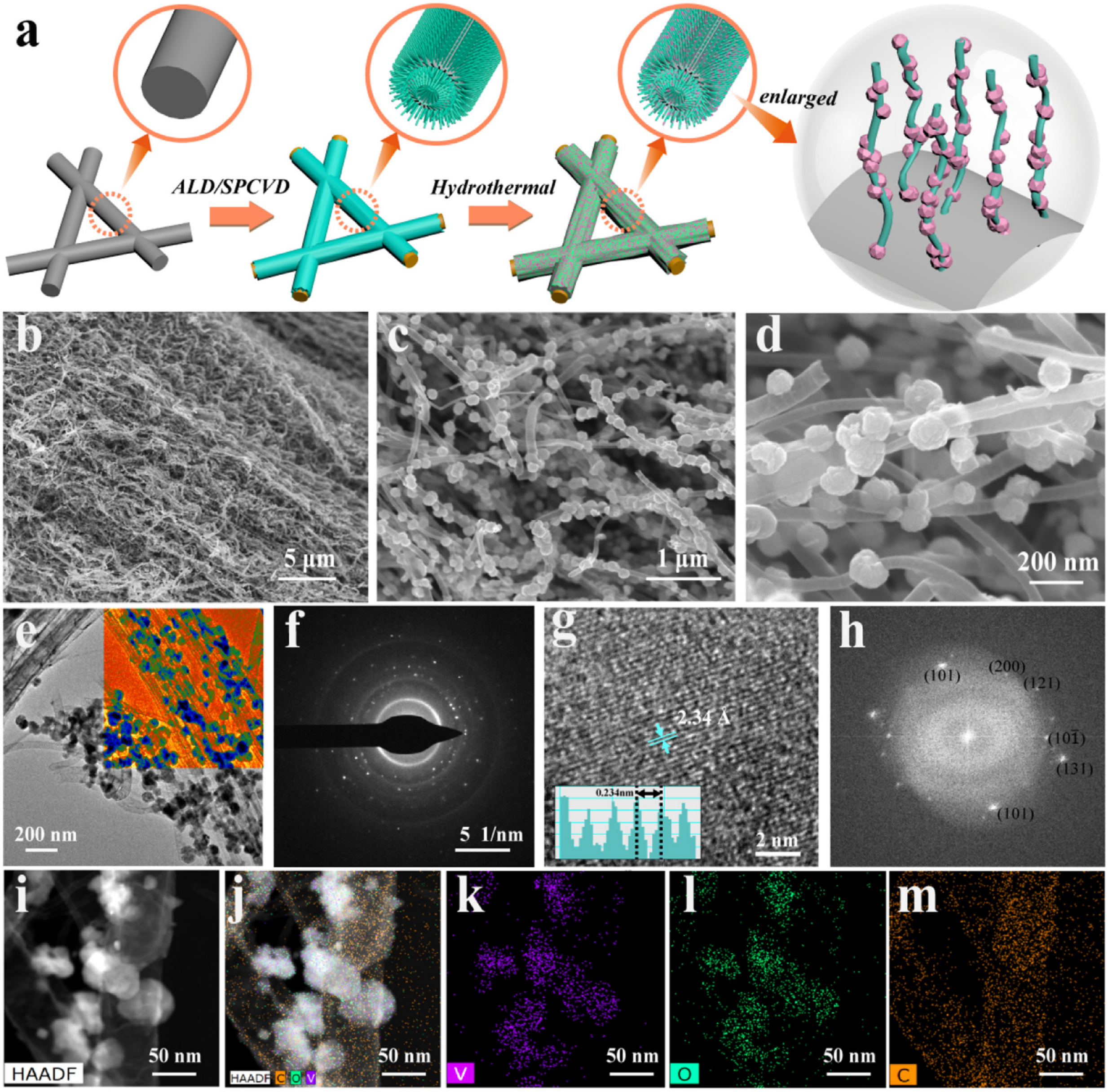

Fig. 1. (a) Schematic illustration of the synthesis of the VO_2(P)-NCNT host; (b–d) FESEM images (e–g) TEM images and SAED pattern; (h) FFT pattern corresponding to (g); (i–m) STEM EDX mapping images of the VO_2(P)-NCNT host.

S10 show the FESEM images and corresponding EDX mapping images of VO_2(P)-NCNT/S cathode after 500 cycles at 2.0 C. The VO_2(P)-NCNT/S cathode after long-term cycling still maintain the original morphology of VO_2(P) nanoparticles on NCNT, suggesting high structural stability of the VO_2(P)-NCNT host.

Despite the remarkable progress made on cycling stability, it should be noted that almost all the long-term cycling performance is achieved with low areal loading sulfur cathodes (usually < 2.0 mg cm^{-2}) [48]. Thus, it is important to attain cathodes with high areal loading (> 4.0 mg cm^{-2}) and long-term cycling life (> 500 cycles) to meet real applications of Li-S batteries. In Fig. 3d, the VO_2(P)-NCNT/S cathode with a sulfur loading of 4.8 mg cm^{-2} shows a high reversible capacity of ~450 mg cm^{-2} and stable cycling performance with a decay rate of about 0.09% per cycle. The electrochemical performance of VO_2(P)-NCNT/S cathodes with high areal loading of 6.4 and 9.6 mg cm^{-2} were also tested (Fig. 3e and Fig. S11). The corresponding galvanostatic charge/discharge tests were shown in Fig. S12. The VO_2(P)-NCNT with sulfur loadings of 6.4 and 9.6 mg cm^{-2} at 0.2 C show high initial areal capacities of 7.8 and 10.2 mAh·cm^{-2}, respectively. It worth noting that the VO_2(P)-NCNT/S cathode of 6.4 and 9.6 mg cm^{-2} maintain high areal capacities of 4.8 and 5.7 mAh·cm^{-2} even after 200 cycles, which are larger than the standard for commercial Lithium-ion batteries (4 mA h cm^{-2}). Performance comparisons with recent work on vanadium-based cathodes in Li-S batteries are shown in Fig. 3f [23,24,35,49–54]. Our work shows as one of the best results reported to date (Table S1). The high sulfur loading VO_2(P)-NCNT/S cathode with high cycling stability and large areal capacity demonstrates its excellent electrochemical performance as a composite host for Li-S batteries.

3.3. Redox kinetics characterizations

Fig. 4a and Fig. S13 display the cyclic voltammograms (CV) of VO_2(P)-NCNT/S and NCNT/S with the same sulfur loading at a scan rate of 0.1 mV s^{-1}, which exhibit the characteristic lithiation/delithiation features of sulfur cathodes. Compared to the NCNT/S cathode, VO_2(P)-NCNT/S shows an obvious shift to a higher potential in the

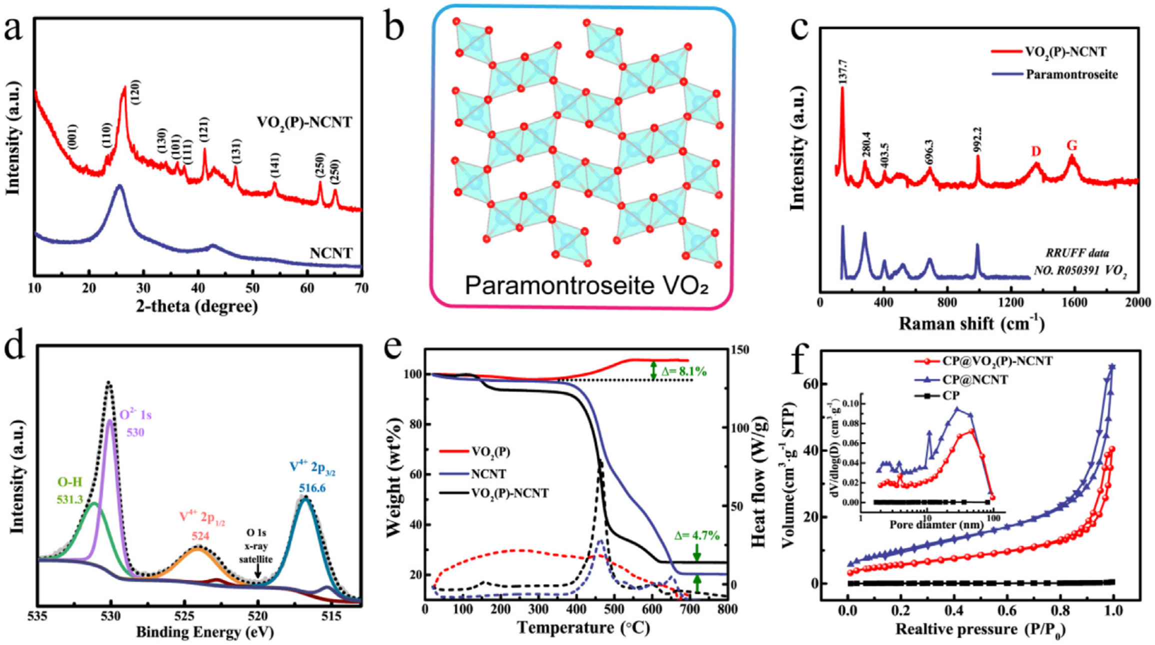

Fig. 2. (a) XRD patterns; (b) schematic illustration of orthorhombic paramontroseite VO_2 projected along [001]; (c) Raman spectra; (d) XPS spectra; (e) TGA/DSC curves, and (f) N_2 adsorption-desorption curves and analysis of the VO_2(P)-NCNT host.

lithiation (discharge) sweep and a negative shift to a lower potential in the delithiation (charge) sweep, indicating a decrease of cell polarization [55]. The potential shifts in charge/discharge sweeps suggest that the redox kinetics reactions in the Li-S battery have been improved by the VO_2(P). The Tafel plots (Fig. S14) and corresponding onset potentials and exchange current densities (Fig. 4b) are determined by potentiostatic polarization experiments [55,56]. The higher onset potential values in the lithiation process and lower values in the delithiation process indicate more favorable reaction kinetics occurring in the VO_2(P)-NCNT/S cathodes. Additionally, the larger exchange current densities of VO_2(P)-NCNT/S cathodes also indicates that the VO_2(P) nanoparticles could effectively accelerate the charge transfer and redox reaction.

To analyze the VO_2(P) on the improvement of the redox kinetics during cycling, the Nyquist plots before/after cycling are measured (Fig. 4c). The Nyquist plots were fitted with an equivalent circuit (inset of Fig. 4b) and the fitting results are summarized in Table S1. The first intercept (at high frequency) corresponds to the electrolyte resistance (R_s). The curve at high frequency is ascribed to Li-ion diffusion through the surface of nanolayers (R_{surf}), the curve at medium frequency is assigned to charge transfer (R_{ct}) and double-layer capacitance (C_{dl}) [57]. The Ohmic resistance of VO_2(P)-NCNT/S and NCNT/S cathodes before/after cycling are similar. In addition, the VO_2(P)-NCNT/S before/after cycling (41.8/87.1 Ω) shows a smaller charge transfer resistance than those of NCNT/S (51.7/111.8 Ω). More importantly, R_{surf} of the VO_2(P)-NCNT/S (23.6 Ω) after cycling is much smaller than that of the pure NCNT/S (75.2 Ω), demonstrating that the VO_2(P) facilitates Li-ion diffusion from the electrolyte to the electrode surface. The slope of the linear fitting plot of Z′ versus $\omega^{-1/2}$ defines the Warburg factor, which reflects the solid-state diffusion of ions inside the electrode materials (see Supporting information for details) [43]. Before cycling, both VO_2(P)-NCNT/S and NCNT/S show similar slopes in Fig. 4d. After cycling, the increased slope of the NCNT/S cathode indicates the decreased ion diffusion coefficient. In contrast, VO_2(P)-NCNT/S still has a small slope. Therefore, it can be concluded that VO_2(P) plays a key role in maintaining fast ion diffusion kinetics.

To operate the cell under almost quasi-equilibrium conditions, the GITT curves are measured for the 1st cycle (Fig. 4e). In a typical process, a current pulse of 0.05 C was applied for 30 min to measure the closed-circuit-voltage (CCV), and then resting for 1 h to obtain the quasi-open-circuit-voltage (QOCV). Compared with the pure NCNT/S, the charge/discharge plateaus of VO_2(P)-NCNT/S are longer and flatter, thus demonstrating larger capacities. In addition, VO_2(P)-NCNT/S shows lower oxidation voltage plateaus and decreased hysteresis (ΔE, voltage gap between oxidation and reduction plateaus), which further reveal the accelerated redox kinetics of VO_2(P)-NCNT/S cathode. To analyze detailed variations during the charge/discharge process, the reaction resistances (R.R.) at different lithiation/delithiation stages were evaluated from the difference between CCV and QOCV (Fig. 4f) [45]. The R.R. of VO_2(P)-NCNT/S are much lower than those of pure NCNT/S and are ascribed to the transfer reactions of $Li_2S_x(x < 4)$ to Li_2S in the discharge process and from $Li_2S_x(x > 6)$ to S_8 in the charge process. These results suggest that VO_2(P) accelerate the redox kinetics of LiPS conversions in VO_2(P)-NCNT/S cathode.

To further identify the redox reaction mechanisms of the cathodes during the charge/discharge process, ex-situ XANES of S K-edge for NCNT and VO_2(P)-NCNT hosts at different states of charge/discharge during the first cycle is shown in Fig. 5. For the S K-edge of NCNT, the intensity of the XANES peak corresponding to S_8 at 2471.5 eV is decreased in the discharge process, which represents the transformation from S_8 to LiPS (Fig. 5a). When discharged to 1.7 V, a low energy peak appears which is derived from the presence of LiPS (Li_2S_x, $x > 2$) and there is no evidence of the formation of insoluble Li_2S. The accumulation of LiPS in electrolyte causes severe shuttle movement to the anode to form non-reusable solid Li_2S_2/Li_2S and thus leads to the irreversible loss of active materials [58].

However, the S K-edge of VO_2(P)-NCNT host shows a typical Li-S reaction process corresponding to the typical 2-plateau charge/discharge voltage profile of Li-S batteries in ether-based electrolytes (Fig. 5b). When discharged to 2.0 V, a typical LiPS peak appears at lower energy of S_8 peak. After the voltage is discharged to 1.7 V, clear Li_2S peaks at 2471.6 and 2473.3 eV [57] form at higher energy of S_8 peak (IV in Fig. 5b). These results indicate that the VO_2(P) accelerate the transformations from the LiPS to insoluble Li_2S. In the charge process, the Li_2S retransform to LiPS at 2.3 V. It should be known that the transformation of insoluble Li_2S back to LiPS also requires a large activation energy because the aggregation during their formation process always leads to the slow reaction kinetics and low energy efficiency

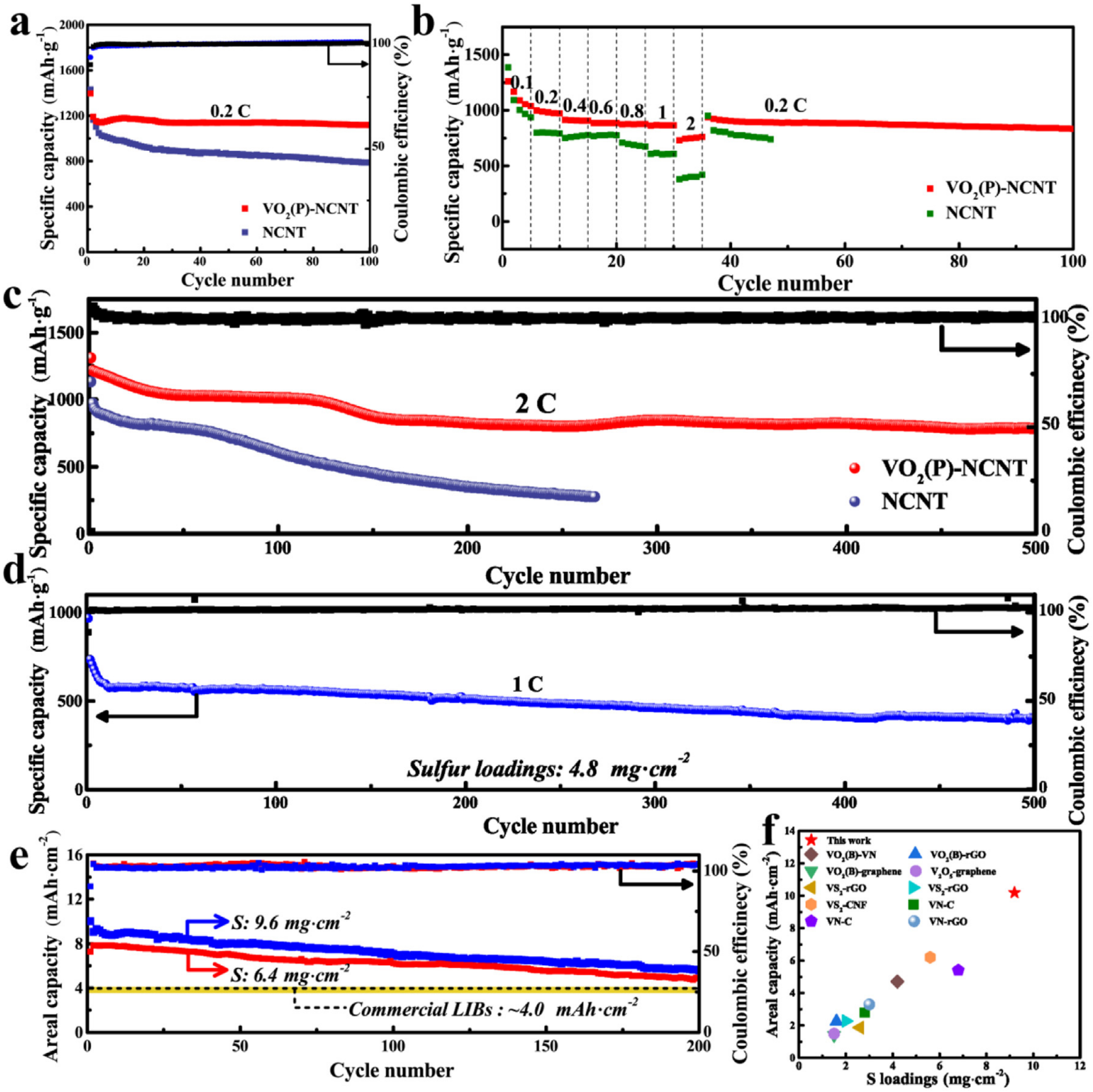

Fig. 3. (a) Cyclic performance at 0.2 C for 100 cycles; (b) Rate capability curves at various current densities from 0.1 C to 2 C; (c) Long-term cycling performance at 2 C for 500 cycles of NCNT/S and VO_2(P)-NCNT/S cathodes; (d) Long-term cycling performance at 1 C for 500 cycles of VO_2(P)-NCNT/S cathodes with a high sulfur loading of 4.8 mg cm^{-2}; (e) Areal capacities of VO_2(P)-NCNT/S cathodes with high sulfur loadings of 6.4 and 9.6 mg cm^{-2}; (f) Comparison of recent work on vanadium-based cathodes in Li-S batteries.

[9,59]. In addition, an S_8 peak with strong intensity was reformed when charged to 2.8 V, which suggests low consumption of active material and superior cycling performance. Even after 300 cycles, the S_8 peak could still be identified.

3.4. Polysulfides conversion characterizations

As LiPS shuttle reactions are the chief culprit for capacity fading and even the failure of Li-S batteries, constructing redox mediators to propel soluble LiPS conversion is one of the best choices to maintain stable electrochemical performance of Li-S batteries [9]. To test the interaction between VO_2(P) and LiPS, Li_2S_4/DME and Li_2S_6/DME solutions were used to test LiPS adsorptions (Fig. 6a). After 30 min, the NCNT appeared to have no observable effect on the Li_2S_4/DME or Li_2S_6/DME solutions since the color remained the same level. However, VO_2(P)-NCNT completely dissolved Li_2S_4 or Li_2S_6 and the solutions became transparent. The obvious contrast suggests a strong affinity between Li_2S_4/Li_2S_6 and VO_2(P) with chemical bonding. Additional visual observation tests in terms of disassembled separators further verify that LPS dissolution into the electrolyte was effectively mitigated by the VO_2(P)-involved cathode. (Fig. S15).

To further identify the LiPS conversion catalyst with VO_2(P), symmetrical cells with two identical electrodes were designed (Fig. 6b). The electrolytes without the addition of Li_2S_6 were also compared. For symmetric batteries without Li_2S_6, the current densities of VO_2(P)-NCNT electrodes are negligible, which implied that the polarization profiles were mainly derived from the redox current of Li_2S_6 (capacitive current caused by the symmetrical electrodes are negligible). For symmetric batteries with Li_2S_6, it can be clearly observed that the current density of VO_2(P)-NCNT electrodes were much larger with obvious redox peaks, demonstrating that VO_2(P) not only electrochemically interact with LiPS but also catalyze the conversion of LiPS. The increased redox current of VO_2(P)-NCNT electrode under a polarization of ± 1.0 V was in good accordance with the EIS results (Fig. S16).

We used X-ray absorption near-edge spectroscopy (XANES), electron energy-loss spectra (EELS), and XPS to determine the variations in the catalyzed polysulfide chains produced by the VO_2(P)-NCNT host. To

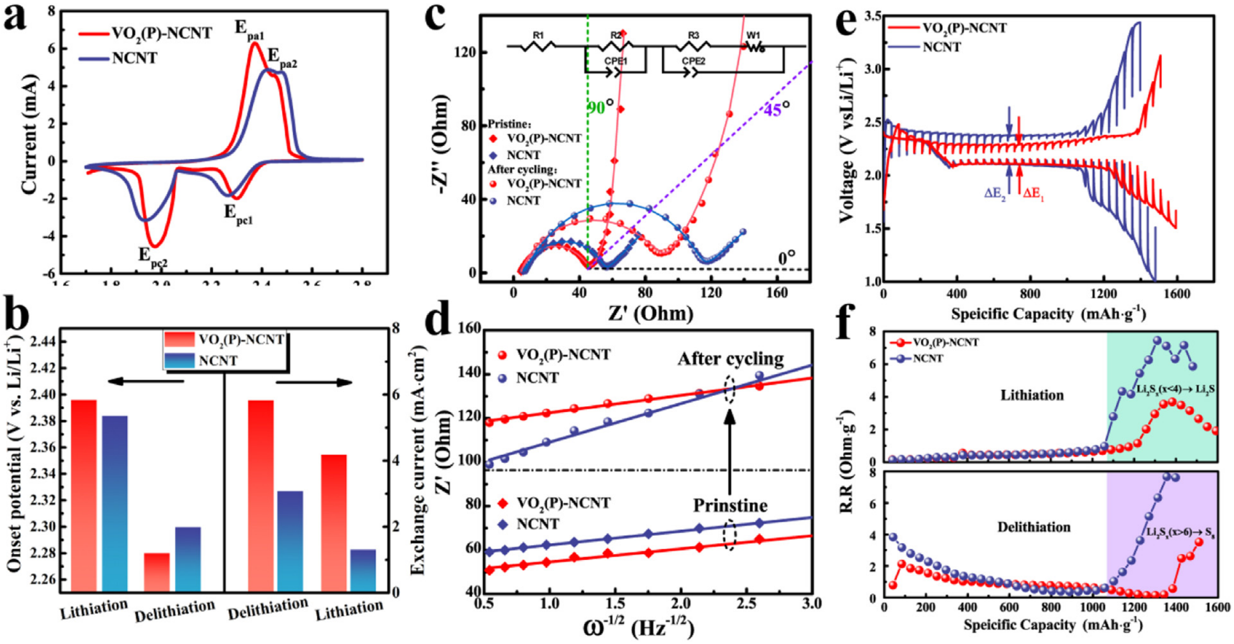

Fig. 4. (a) Cyclic voltammetry curves at a scanning rate of 0.1 mV s^{-1}; (b) Comparison of the onset potentials and the derived exchange current densities for lithiation/delithiation reactions. (c) EIS curves; (d) The relationship between Z′ and $\omega^{-1/2}$ with frequency range between 1 and 0.01 Hz before/after cycling (symbols, real data; lines, fitting curves) (e) GITT curves for first charge/discharge process; (f) reaction resistances during the charge/discharge process of NCNT/S and VO$_2$(P)-NCNT/S cathodes.

avoid the interference derived from functional groups and charge/discharge products in the electrolyte, we used Li_2S_4, a probe species that represents a polysulfide at an average depth of discharge, to investigate the products. In Fig. 6c, V K-edge peaks shift to a lower energy after soaking in Li_2S_4-DME solution. The enlarged Fig. (inset of Fig. 6c) shows that the pre-edge peak shifts from 5468.46 to 5467.75 eV, indicating that the V^{4+} in VO$_2$(P) is partly reduced to V^{3+}. The V K-edge of standard commercial V_2O_3 is shown in Fig. S17, which is consistent with the peak position of VO$_2$(P)-NCNT/Li_2S_4. Similarly, the V L_3-edge of EELS shifts from 524.9 to 523 eV, indicating that the valance of vanadium shifts to a lower state (Fig. 6d) [45]. Compared with the pristine state, two new peaks appear at 2478.8 and 2479.9 eV in the sulfur K-edge curves, which correspond to the thiosulfate ($S_2O_3^{2-}$) [60]. These two peaks are adequately verified by the curve of standard commercial $Na_2S_2O_3$ (inset in Fig. 6e). Similarly, the S 2p peaks of VO$_2$(P)-NCNT/Li_2S_4 (2p3/2 at 168.2 eV, 2p1/2 at 167.1 eV) are also attributed to $S_2O_3^{2-}$ (Fig. 6f) [61]. In this case, VO$_2$(P) particles that are attached to conductive NCNT arrays provide access for electric charge to reach the VO$_2$(P)-LiPS interface and to trigger LiPS redox reactions. As reported by the previous references [11,35], elemental sulfur undergoes nucleophilic attack by $S_2O_3^{2-}$ and form chains of LiPS or polythionate complexes, which is known as the 'Wackenroder reaction'. In this way, the insoluble $S_2O_3^{2-}$ that forms on the surface acts as an internal mediator to anchor long-chain LiPS from solution and to trigger conversion to low-order Li_2S_2/Li_2S [35].

The schematic illustration of VO$_2$(P) driving LiPS conversion by thiosulfate–polythionate with appropriate redox potentials are summarized in Fig. 6g. First, VO$_2$(P) nanoparticles act as catalysts to oxidize the LiPS to produce thiosulfate due to the strong interaction between VO$_2$(P) and LiPS. Second, thiosulfates act as a mediator to catenate long-chain Li_2S_x ($x \geq 4$) and produce short-chain Li_2S_2/Li_2S and surface-bound polythionate complexes. Thus, the VO$_2$(P) plays a vital role in LiPS conversion to polythionate [O_3S_2–$(S)_{x-2}$–S_2O_3] to suppress the LiPS shuttle reactions, resulting in Li-S batteries with superior

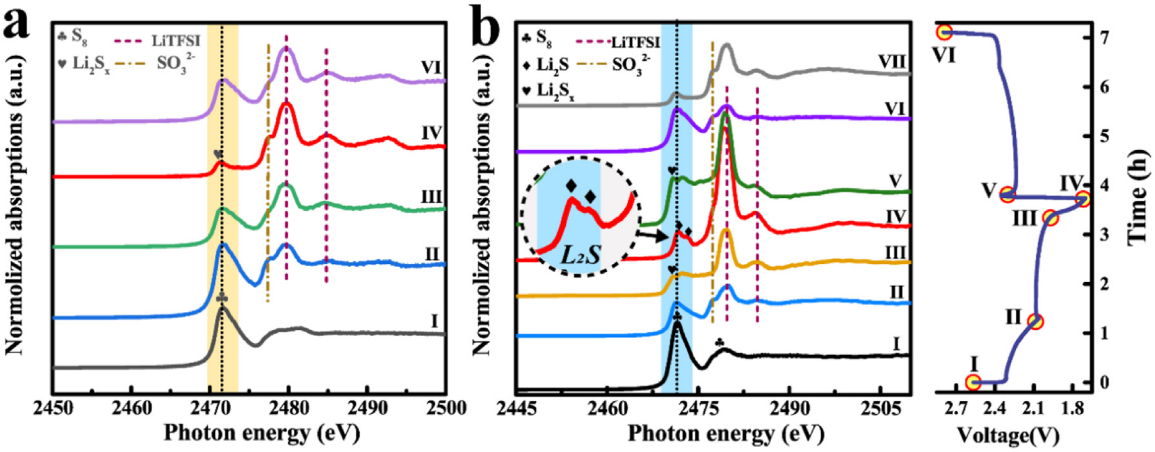

Fig. 5. *Ex-situ* XANES of S K-edge for (a) NCNT/S and (b) VO$_2$(P)-NCNT/S cathodes at certain states of charge/discharge during the first cycle, (i) pristine, (ii) first discharge to 2.1 V, (iii) first discharge to 2.0 V, (iv) first discharge to 1.7 V, (v) first charge to 2.3 V, (vi) first charge to 2.8 V, and (vii) after 300 cycles at 2.8 V.

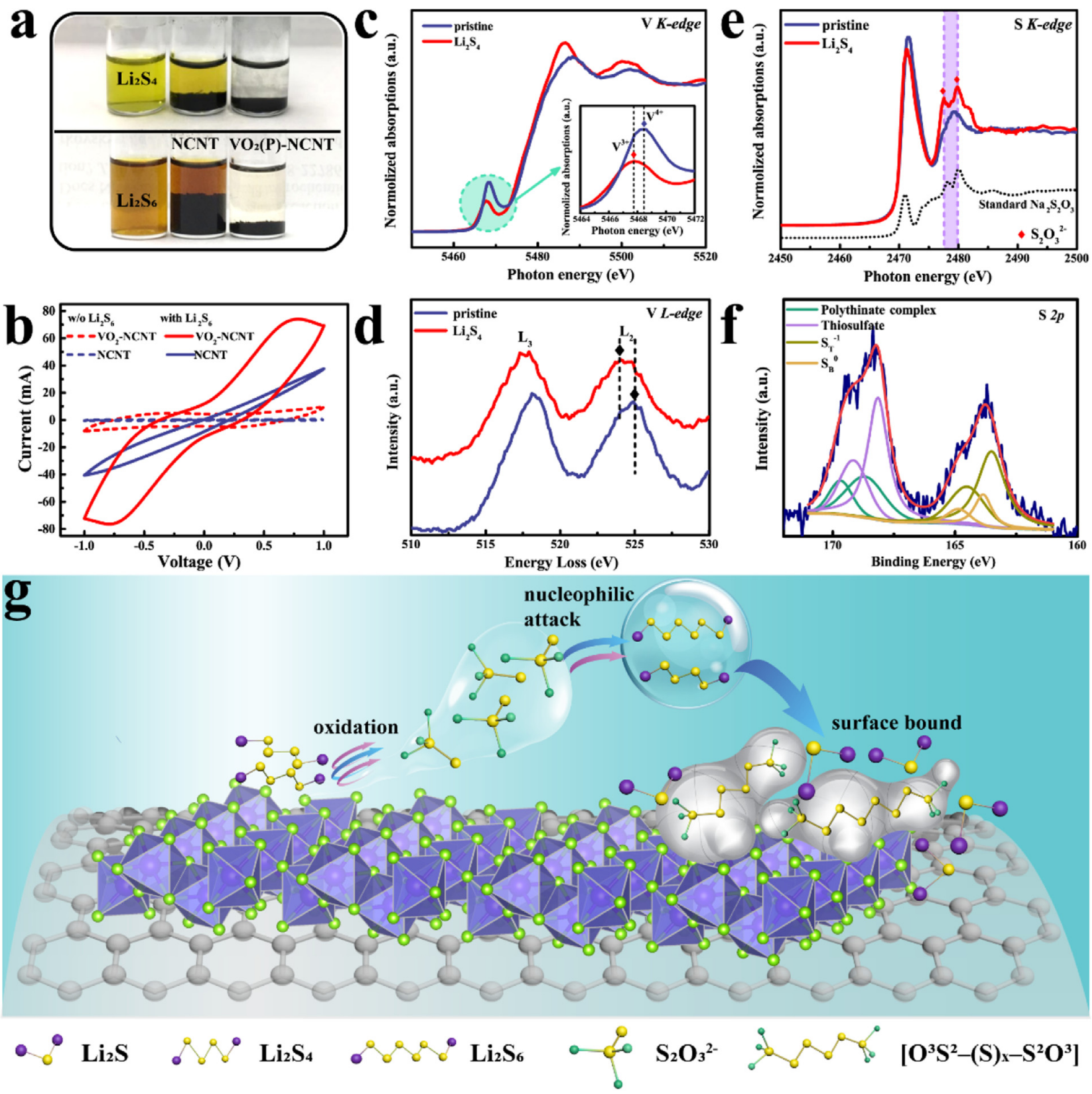

Fig. 6. (a) Adsorption properties of NCNT and VO_2(P)-NCNT in Li_2S_4 and Li_2S_6 solutions; (b) Cyclic voltammograms of symmetric cells with identical electrodes of NCNT and VO_2(P)-NCNT electrodes in electrolytes with/without Li_2S_6 at 50 mV s^{-1}. (c) The XANES of V K-edge (d) EELS of V L-edge; (e) The XANES of S K-edge curves; (f) XPS of S 2p peaks of pristine and VO_2(P)-NCNT/Li_2S_4 samples; (g) Schematic illustration of trapping polysulfides by thiosulfate–polythionate conversion for VO_2(P) with appropriate redox potentials.

performance.

4. Conclusion

A composite host consisting of uniform VO_2(P) nanoparticles grown on parallel NCNT arrays result in a 3D free-standing hierarchical structure. In this host, VO_2(P) nanoparticles not only accelerate the charge transfer and ion diffusion with fast redox kinetics but also catalyze the conversion of soluble long-chain LiPS to insoluble polythionate complexes and short-chain Li_2S_2/Li_2S, thus effectively suppressing the shuttle reaction for stable cycling performance. The VO_2(P)-NCNT/S cathodes exhibits excellent performance with high reversible discharge capacity (≈1200 mA h g^{-1} at 0.2 C), stable long-term cycling (≈67% retention at 2 C for 500 cycles), and high sulfur loading cycling (initial areal capacity of 10.2 mA h cm^{-2} at 0.2 C for 200 cycles). This study demonstrates that the introduction of VO_2(P) enables the design of high loading sulfur-based cathodes with high performance by catalyzing the conversion of LiPS, and has potential applications for the development of practical Li-S batteries.

Acknowledgements

This research was supported by the Natural Science and Engineering Research Council of Canada (NSERC), the Canada Research Chair Program (CRC), the Canada Foundation for Innovation (CFI), and the Western University, National Natural Science Foundation of China of 51172034, the National Defense Science and Technology Innovation Special Zone project of 17-163-13-ZT-009-125-001, and the International cooperation projects of Sichuan Provincial Department of Science and Technology of 2017HH0067 and 2017HH0101. Sizhe Wang is supported by the Chinese Scholarship Council. The electron microscopy (S.Z.Y.) was supported in part by the U.S. Department of

Energy, Office of Science, Basic Energy Sciences, Materials Science, and Engineering Division Part of the Electron Microscopy. This research used resources of the Center for Functional Nanomaterials, which is a U.S. DOE Office of Science Facility, at Brookhaven National Laboratory under Contract No. DE-SC0012704.

Appendix A. Supplementary material

Supplementary data associated with this article can be found in the online version at doi:10.1016/j.nanoen.2018.12.020.

References

[1] Z.W. Seh, Y. Sun, Q. Zhang, Y. Cui, Designing high-energy lithium-sulfur batteries, Chem. Soc. Rev. 45 (20) (2016) 5605–5634.
[2] X. Yang, X. Li, K. Adair, H. Zhang, X. Sun, Structural design of lithium–sulfur batteries: from fundamental research to practical application, Electrochem. Energy Rev. (2018).
[3] Q. Pang, X. Liang, C.Y. Kwok, L.F. Nazar, Advances in lithium–sulfur batteries based on multifunctional cathodes and electrolytes, Nat. Energy 1 (9) (2016) 16132.
[4] H.J. Peng, J.Q. Huang, Q. Zhang, A review of flexible lithium-sulfur and analogous alkali metal-chalcogen rechargeable batteries, Chem. Soc. Rev. 46 (17) (2017) 5237–5288.
[5] X. Yang, H. Zhang, Y. Chen, Y. Yu, X. Li, H. Zhang, Shapeable electrodes with extensive materials options and ultra-high loadings for energy storage devices, Nano Energy 39 (2017) 418–428.
[6] X. Yang, Y. Chen, M. Wang, H. Zhang, X. Li, H. Zhang, Phase inversion: a universal method to create high-performance porous electrodes for nanoparticle-based energy storage devices, Adv. Funct. Mater. 26 (46) (2016) 8427–8434.
[7] X. Liu, J.Q. Huang, Q. Zhang, L. Mai, Nanostructured metal oxides and sulfides for lithium-sulfur batteries, Adv. Mater. 29 (20) (2017).
[8] J. Xu, T. Lawson, H. Fan, D. Su, G. Wang, Updated metal compounds (MOFs, □S, □OH, □N, □C) used as cathode materials for lithium-sulfur batteries, Adv. Energy Mater. (2018) 1702607.
[9] D. Liu, C. Zhang, G. Zhou, W. Lv, G. Ling, L. Zhi, Q.H. Yang, Catalytic effects in lithium-sulfur batteries: promoted sulfur transformation and reduced shuttle effect, Adv. Sci. 5 (1) (2018) 1700270.
[10] Q. Pang, D. Kundu, M. Cuisinier, L.F. Nazar, Surface-enhanced redox chemistry of polysulphides on a metallic and polar host for lithium-sulphur batteries, Nat. Commun. 5 (2014) 4759.
[11] X. Liang, C. Hart, Q. Pang, A. Garsuch, T. Weiss, L.F. Nazar, A highly efficient polysulfide mediator for lithium-sulfur batteries, Nat. Commun. 6 (2015) 5682.
[12] C. Zheng, S. Niu, W. Lv, G. Zhou, J. Li, S. Fan, Y. Deng, Z. Pan, B. Li, F. Kang, Q.-H. Yang, Propelling polysulfides transformation for high-rate and long-life lithium–sulfur batteries, Nano Energy 33 (2017) 306–312.
[13] L. Kong, X. Chen, B.Q. Li, H.J. Peng, J.Q. Huang, J. Xie, Q. Zhang, A bifunctional perovskite promoter for polysulfide regulation toward stable lithium-sulfur batteries, Adv. Mater. (2017).
[14] D. Xiao, C. Lu, C. Chen, S. Yuan, CeO2-webbed carbon nanotubes as a highly efficient sulfur host for lithium-sulfur batteries, Energy Storage Mater. 10 (2018) 216–222.
[15] Y. Chen, S. Choi, D. Su, X. Gao, G. Wang, Self-standing sulfur cathodes enabled by 3D hierarchically porous titanium monoxide-graphene composite film for high-performance lithium-sulfur batteries, Nano Energy 47 (2018) 331–339.
[16] J. Xu, W. Zhang, Y. Chen, H. Fan, D. Su, G. Wang, MOF-derived porous N–Co 3 O 4@ N–C nanododecahedra wrapped with reduced graphene oxide as a high capacity cathode for lithium–sulfur batteries, J. Mater. Chem. A 6 (6) (2018) 2797–2807.
[17] Z. Yuan, H.J. Peng, T.Z. Hou, J.Q. Huang, C.M. Chen, D.W. Wang, X.B. Cheng, F. Wei, Q. Zhang, Powering lithium-sulfur battery performance by propelling polysulfide redox at sulfiphilic hosts, Nano Lett. 16 (1) (2016) 519–527.
[18] H. Lin, L. Yang, X. Jiang, G. Li, T. Zhang, Q. Yao, G.W. Zheng, J.Y. Lee, Electrocatalysis of polysulfide conversion by sulfur-deficient MoS2 nanoflakes for lithium–sulfur batteries, Energy Environ. Sci. 10 (6) (2017) 1476–1486.
[19] J. Pu, Z. Shen, J. Zheng, W. Wu, C. Zhu, Q. Zhou, H. Zhang, F. Pan, Multifunctional Co 3 S 4 @sulfur nanotubes for enhanced lithium-sulfur battery performance, Nano Energy 37 (2017) 7–14.
[20] G. Zhou, H. Tian, Y. Jin, X. Tao, B. Liu, R. Zhang, Z.W. Seh, D. Zhuo, Y. Liu, J. Sun, J. Zhao, C. Zu, D.S. Wu, Q. Zhang, Y. Cui, Catalytic oxidation of Li2S on the surface of metal sulfides for Li-S batteries, Proc. Natl. Acad. Sci. USA 114 (5) (2017) 840–845.
[21] J. Xu, W. Zhang, H. Fan, F. Cheng, D. Su, G. Wang, Promoting lithium polysulfide/sulfide redox kinetics by the catalyzing of zinc sulfide for high performance lithium-sulfur battery, Nano Energy (2018).
[22] T. Zhou, W. Lv, J. Li, G. Zhou, Y. Zhao, S. Fan, B. Liu, B. Li, F. Kang, Q.-H. Yang, Twinborn TiO 2–tin heterostructures enabling smooth trapping–diffusion–conversion of polysulfides towards ultralong life lithium–sulfur batteries, Energy Environ. Sci. 10 (7) (2017) 1694–1703.
[23] Z. Sun, J. Zhang, L. Yin, G. Hu, R. Fang, H.M. Cheng, F. Li, Conductive porous vanadium nitride/graphene composite as chemical anchor of polysulfides for lithium-sulfur batteries, Nat. Commun. 8 (2017) 14627.
[24] Y. Song, W. Zhao, L. Kong, L. Zhang, X. Zhu, Y. Shao, F. Ding, Q. Zhang, J. Sun, Z. Liu, Synchronous immobilization and conversion of polysulfides on VO 2-VN binary host targeting high sulfur loading Li–S batteries, Energy Environ. Sci. (2018).
[25] F. Zhou, Z. Li, X. Luo, T. Wu, B. Jiang, L.L. Lu, H.B. Yao, M. Antonietti, S.H. Yu, Low cost metal carbide nanocrystals as binding and electrocatalytic sites for high performance Li-S batteries, Nano Lett. 18 (2) (2018) 1035–1043.
[26] K. Park, J.H. Cho, J.-H. Jang, B.-C. Yu, A.T. De. La Hoz, K.M. Miller, C.J. Ellison, J.B. Goodenough, Trapping lithium polysulfides of a Li–S battery by forming lithium bonds in a polymer matrix, Energy Environ. Sci. 8 (8) (2015) 2389–2395.
[27] L. Li, L. Chen, S. Mukherjee, J. Gao, H. Sun, Z. Liu, X. Ma, T. Gupta, C.V. Singh, W. Ren, H.M. Cheng, N. Koratkar, Phosphorene as a polysulfide immobilizer and catalyst in high-performance lithium-sulfur batteries, Adv. Mater. 29 (2) (2017).
[28] T.Z. Hou, W.T. Xu, X. Chen, H.J. Peng, J.Q. Huang, Q. Zhang, Lithium bond chemistry in lithium–sulfur batteries, Angew. Chem. Int. Ed. 56 (28) (2017) 8178–8182.
[29] L.-C. Yin, J. Liang, G.-M. Zhou, F. Li, R. Saito, H.-M. Cheng, Understanding the interactions between lithium polysulfides and N-doped graphene using density functional theory calculations, Nano Energy 25 (2016) 203–210.
[30] D. Su, M. Cortie, G. Wang, Fabrication of N-doped graphene–carbon nanotube hybrids from Prussian blue for lithium–sulfur batteries, Adv. Energy Mater. 7 (8) (2017) 1602014.
[31] D. Su, M. Cortie, H. Fan, G. Wang, Prussian blue nanocubes with an open framework structure coated with PEDOT as high-capacity cathodes for lithium-sulfur batteries, Adv. Mater. 29 (48) (2017).
[32] C. Wu, F. Feng, Y. Xie, Design of vanadium oxide structures with controllable electrical properties for energy applications, Chem. Soc. Rev. 42 (12) (2013) 5157–5183.
[33] K. Liu, S. Lee, S. Yang, O. Delaire, J. Wu, Recent progresses on physics and applications of vanadium dioxide, Mater. Today (2018).
[34] M. Liu, B. Su, Y. Tang, X. Jiang, A. Yu, Recent advances in nanostructured vanadium oxides and composites for energy conversion, Adv. Energy Mater. 7 (23) (2017) 1700885.
[35] X. Liang, C.Y. Kwok, F. Lodi-Marzano, Q. Pang, M. Cuisinier, H. Huang, C.J. Hart, D. Houtarde, K. Kaup, H. Sommer, T. Brezesinski, J. Janek, L.F. Nazar, Tuning transition metal oxide-sulfur interactions for long life lithium sulfur batteries: the “Goldilocks” principle, Adv. Energy Mater. 6 (6) (2016) 1501636.
[36] Y. Song, W. Zhao, L. Kong, L. Zhang, X. Zhu, Y. Shao, F. Ding, Q. Zhang, J. Sun, Z. Liu, Synchronous immobilization and conversion of polysulfides on a VO 2–VN binary host targeting high sulfur load Li–S batteries, Energy Environ. Sci. (2018).
[37] S. Zhang, B. Shang, J. Yang, W. Yan, S. Wei, Y. Xie, From VO2 (B) to VO2 (A) nanobelts: first hydrothermal transformation, spectroscopic study and first principles calculation, Phys. Chem. Chem. Phys.: PCCP 13 (35) (2011) 15873–15881.
[38] Y. Zhang, VO2(B) conversion to VO2(A) and VO2(M) and their oxidation resistance and optical switching properties, Mater. Sci. 34 (1) (2016).
[39] C. Wu, F. Feng, J. Feng, J. Dai, J. Yang, Y. Xie, Ultrafast solid-state transformation pathway from new-phased goethite VOOH to paramontroseite VO2 to rutile VO2 (R), J. Phys. Chem. C 115 (3) (2010) 791–799.
[40] H. Evans, M.E. Mrose, A crystal chemical study of montroseite and paramontroseite, Am. Mineral. 40 (9–10) (1955) 861–875.
[41] C. Wu, Z. Hu, W. Wang, M. Zhang, J. Yang, Y. Xie, Synthetic paramontroseite VO2 with good aqueous lithium-ion battery performance, Chem. Commun. (33) (2008) 3891–3893.
[42] H. Yadegari, M.N. Banis, B. Xiao, Q. Sun, X. Li, A. Lushington, B. Wang, R. Li, T.-K. Sham, X. Cui, X. Sun, Three-dimensional nanostructured air electrode for sodium–oxygen batteries: a mechanism study toward the cyclability of the cell, Chem. Mater. 27 (8) (2015) 3040–3047.
[43] S. Wang, J. Liao, M. Wu, Z. Xu, F. Gong, C. Chen, Y. Wang, X. Yan, High rate and long cycle life of a CNT/rGO/Si nanoparticle composite anode for lithium-ion batteries, Part. Part. Syst. Charact. 34 (10) (2017) 1700141.
[44] Y. Song, J. Liao, C. Chen, J. Yang, J. Chen, F. Gong, S. Wang, Z. Xu, M. Wu, Controllable morphologies and electrochemical performances of self-assembled nano-honeycomb WS 2 anodes modified by graphene doping for lithium and sodium ion batteries, Carbon (2018).
[45] S. Wang, F. Gong, S. Yang, J. Liao, M. Wu, Z. Xu, C. Chen, X. Yang, F. Zhao, B. Wang, Y. Wang, X. Sun, Graphene oxide-template controlled cuboid-shaped high-capacity VS4 nanoparticles as anode for sodium-ion batteries, Adv. Funct. Mater. (2018) 1801806.
[46] J. Mendialdua, R. Casanova, Y. Barbaux, XPS studies of V2O5, V6O13, VO2 and V2O3, J. Electron Spectrosc. Relat. Phenom. 71 (3) (1995) 249–261.
[47] A. Dhayal Raj, T. Pazhanivel, P. Suresh Kumar, D. Mangalaraj, D. Nataraj, N. Ponpandian, Self assembled V2O5 nanorods for gas sensors, Curr. Appl. Phys. 10 (2) (2010) 531–537.
[48] L. Qie, A. Manthiram, High-energy-density lithium–sulfur batteries based on blade-cast pure sulfur electrodes, ACS Energy Lett. 1 (1) (2016) 46–51.
[49] Y. Song, W. Zhao, X. Zhu, L. Zhang, Q. Li, F. Ding, Z. Liu, J. Sun, Vanadium dioxide-graphene composite with ultrafast anchoring behavior of polysulfides for lithium–sulfur batteries, ACS Appl. Mater. Interfaces 10 (18) (2018) 15733–15741.
[50] X. Zhu, W. Zhao, Y. Song, Q. Li, F. Ding, J. Sun, L. Zhang, Z. Liu, In situ assembly of 2D conductive vanadium disulfide with graphene as a high-sulfur-loading host for lithium-sulfur batteries, Adv. Energy Materials (2018) 1800201.
[51] Z. Cheng, Z. Xiao, H. Pan, S. Wang, R. Wang, Elastic sandwich-type rGO-VS2/S composites with high tap density: structural and chemical cooperativity enabling lithium-sulfur batteries with high energy density, Adv. Energy Mater. (2017) 1702337.
[52] X. Li, K. Ding, B. Gao, Q. Li, Y. Li, J. Fu, X. Zhang, P.K. Chu, K. Huo, Freestanding carbon encapsulated mesoporous vanadium nitride nanowires enable highly stable sulfur cathodes for lithium-sulfur batteries, Nano Energy 40 (2017) 655–662.
[53] L. Ma, H. Yuan, W. Zhang, G. Zhu, Y. Wang, Y. Hu, P. Zhao, R. Chen, T. Chen, J. Liu,

Z. Hu, Z. Jin, Porous-shell vanadium nitride nanobubbles with ultrahigh areal sulfur loading for high-capacity and long-life lithium-sulfur batteries, Nano Lett. 17 (12) (2017) 7839–7846.

[54] L. Wang, Y.-B. He, L. Shen, D. Lei, J. Ma, H. Ye, K. Shi, B. Li, F. Kang, Ultra-small self-discharge and stable lithium-sulfur batteries achieved by synergetic effects of multicomponent sandwich-type composite interlayer, Nano Energy 50 (2018) 367–375.

[55] K. Xu, X. Liu, J. Liang, J. Cai, K. Zhang, Y. Lu, X. Wu, M. Zhu, Y. Liu, Y. Zhu, G. Wang, Y. Qian, Manipulating the redox kinetics of Li–S chemistry by tellurium doping for improved Li–S batteries, ACS Energy Lett. 3 (2) (2018) 420–427.

[56] J. Miao, F.-X. Xiao, H.B. Yang, S.Y. Khoo, J. Chen, Z. Fan, Y.-Y. Hsu, H.M. Chen, H. Zhang, B. Liu, Hierarchical Ni-Mo-S nanosheets on carbon fiber cloth: a flexible electrode for efficient hydrogen generation in neutral electrolyte, Sci. Adv. 1 (7) (2015) e1500259.

[57] G. Tan, R. Xu, Z. Xing, Y. Yuan, J. Lu, J. Wen, C. Liu, L. Ma, C. Zhan, Q. Liu, T. Wu, Z. Jian, R. Shahbazian-Yassar, Y. Ren, D.J. Miller, L.A. Curtiss, X. Ji, K. Amine, Burning lithium in CS2 for high-performing compact Li2S–graphene nanocapsules for Li–S batteries, Nat. Energy 2 (7) (2017) 17090.

[58] Y. Wang, X. Huang, S. Zhang, Y. Hou, Sulfur hosts against the shuttle effect, Small Methods (2018) 1700345.

[59] Z.W. Zhang, H.J. Peng, M. Zhao, J.Q. Huang, Heterogeneous/homogeneous mediators for high-energy-density lithium-sulfur batteries: progress and prospects, Adv. Funct. Mater. 28 (38) (2018) 1707536.

[60] Y. Kitajima, Recent performances of the soft X-ray crystal monochromator stations BL-2A and BL-11B with new focusing mirrors at the Photon Factory, J. Electron Spectrosc. Relat. Phenom. 80 (1996) 405–408.

[61] H. Peisert, T. Chassé, P. Streubel, A. Meisel, R. Szargan, Relaxation energies in XPS and XAES of solid sulfur compounds, J. Electron Spectrosc. Relat. Phenom. 68 (1994) 321–328.

Sizhe Wang is currently a Ph.D. candidate at School of materials and energy, University of Electronic Science and Technology of China (UESTC), China. At the same time, he is a visiting student in Prof. Xueliang (Andy) Sun's Nanomaterials and Energy Group at University of Western Ontario, Canada. He got his B.S. degree in Electronics Science and Technology from School of Microelectronics and Solid-State Electronics, UESTC, in 2013. Currently, his research interests focus on nanocarbon and advanced functional materials as well as their applications in energy conversion and storage, especially for Na/Li-ion batteries and Li-S batteries.

Prof. Jiaxuan Liao is working as a Full professor and a Ph.D. supervisor in University of Electronic Science and Technology of China (UESTC), China. He received his Ph.D. in Materials Science and Engineering in 2001 from Harbin Institute of Technology, and worked as a postdoctoral fellow at Lanzhou Institute of Chemical Physics of Chinese Academy of Sciences in 2003. His current research interests are focused on electronic information materials and devices, electronic functional materials and devices, electronic thin films and integrated devices and new energy materials and devices.

Dr. Xiaofei Yang is currently a postdoctoral associate in Prof. Xueliang (Andy) Sun's Nanomaterials and Energy Group. He received his B.E. degree in Chemical Engineering from Anhui University, China, in 2013 and Ph.D degree in Dalian Institute of Chemical Physics, Chinese Academy of Sciences, China, in 2018 under the supervision of Prof. Huamin Zhang. His research interests focus on Li-S batteries, all-solid-state Li-S batteries and battery interface studies via synchrotron X-ray characterizations.

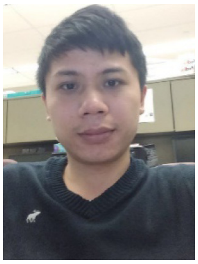

Jianneng Liang is currently a Ph.D. candidate in the department of Mechanical and Materials Engineering at the University of Western Ontario, Canada. He got his B.S. in metallurgical engineering in 2015 from Central South University, China. Currently, his research interests include solid-state polymer electrolytes, hybrid electrolyte, all-solid-state LIBs and Li-S batteries, and the interfacial study in all-solid-state batteries.

Dr. Qian Sun is a postdoctoral associate in Prof. Xueliang (Andy) Sun's Group at the University of Western Ontario (Western University), Canada. He received his B.S. degree in Chemistry in 2006, M.S. degree in Physical Chemistry in 2009, and Ph.D. degree in Applied Chemistry in 2013 under the supervision of Prof. Dr. Zheng-Wen Fu on the study of Li-/Na-ion batteries and Na-air batteries, all at Fudan University, China. He joined Prof. Sun's group in 2013 and his current research interests focus on Na-air, Na-ion, and room temperature Na-S batteries as well as solid-state Li/Na batteries.

Dr. Jianwen Liang received his Ph.D. degree in inorganic chemistry from University of Science and Technology of China in 2015. He is currently a postdoctoral fellow in Prof. Xueliang (Andy) Sun' Nanomaterials and Energy Group at the University of Western Ontario, Canada. His research interests include sulfide-based solid-state electrolyte as well as all-solid-state Li/Li-ion batteries.

Feipeng Zhao is currently a Ph.D. candidate in Prof. Xueliang (Andy) Sun's Group at the University of Western Ontario, Canada. He received his B.S. degree and M.S. degree in Materials Science from Soochow University in 2017 and 2014, respectively. Currently, he is working on the synthesis and characterization of sulfide electrolytes, and development of high-performance solid-state Li metal and Na metal batteries.

Alicia Koo received her B.Sc. in Chemistry at the University of British Columbia in 2016. Her research interests include energy conversion and storage materials for green energy applications. In addition, she is an avid science communicator and advocate for women in STEM.

Fanpeng Kong is currently a Ph.D. candidate under the supervision of Prof. Geping Yin in Harbin Institute of Technology (HIT), China. At the same time, he is a visiting student at Prof. Xueliang (Andy) Sun's Advanced Materials for Clean Energy Group, Western University, Canada. He received his B.E. at HIT in 2014, and then joined Prof. Geping Yin's group at HIT. His current research interest focuses on the design and preparation of single atom and nanomaterials for oxygen reduction, hydrogen evolution and organic small molecular oxidation.

Yao Yao is currently a Ph.D. candidate in National and Local Joint Engineering Laboratory for Lithium-ion Batteries and Materials Preparation Technology at Kunming University of Science and Technology, China. He received his B.S. degree and M.S. degree in Physical Chemistry of Metallurgy from Kunming University of Science and Technology (Kunming, China) in 2012 and 2016, respectively. As a visiting student, he studied in Prof. Xueliang (Andy) Sun's Group at the University of Western Ontario from 2017 to 2018. His current research interests focus on surface modification of electrode materials for lithium/sodium ion batteries.

Xuejie Gao is currently a Ph.D. candidate in Prof. Xueliang (Andy) Sun's group at the University of Western Ontario, Canada. She received her B.S. degree in chemistry in 2014 from Ludong University and obtained her M.S. degree in Chemistry in 2017 from Soochow University. Currently, her research interests focus on the development of 3D printing applied for lithium batteries. She is also co-supervised by Prof. T. K. Sham from Chemistry Department in the University of Western Ontario. Part of her work is related to the study of energy materials via synchrotron radiation.

Prof. Mengqiang Wu is a director of the Center for Advanced Electric Energy Technologies within the School of Materials and Energy and Full Professor at the University of Electronic Science and Technology of China (UESTC), China. He received his M.S. degree in Physical Chemistry from Sichuan University, China and Ph.D. in Microelectronics and Solid-State Electronics from UESTC in 1995 and 2002, respectively. He has been working as a visiting scientist within the University of Cambridge, UK and the University of Nottingham, UK, respectively, and a postdoctoral fellow at the University of Southampton, UK. His current research interests are focused on advanced materials for electrochemical energy storage and conversion, electrodes in lithium-ion batteries, supercapacitors and alkali metal-chalcogen batteries.

Dr. Shize Yang received his Ph.D. degree in condensed matter physics from Peking University in 2014 and then worked as postdoc at Oak Ridge National Laboratory and Brookhaven National Laboratory. His current research interests are focused on electron microscopy techniques including aberration corrected scanning transmission electron microscopy, multidimensional electron tomography, cryogenic electron microscopy and in-situ/environmental electron microscopy. The related material systems range from 2D dimensional monolayers, oxide nanoparticles and metal alloys for applications in energy conversion, catalysis and electronic devices.

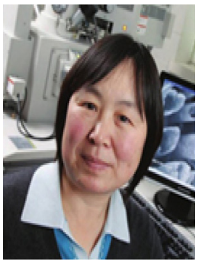

Ruying Li is a research engineer at Prof. Xueliang (Andy) Sun's Nanomaterial and Energy Group at the University of Western Ontario, Canada. She received her master in Material Chemistry under the direction of Prof. George Thompson in 1999 at University of Manchester, UK, followed by work as a research assistant under the direction of Prof. Keith Mitchell at the University of British Columbia and under the direction of Prof. Jean-Pol Dodelet at I′Institut national de la recherché Scientifique (INRS), Canada. Her current research interests are associated with synthesis and characterization of nanomaterials for electrochemical energy storage and conversion.

Prof. Xueliang (Andy) Sun is a Canada Research Chair in Development of Nanomaterials for Clean Energy, Fellow of the Royal Society of Canada and Canadian Academy of Engineering and Full Professor at the University of Western Ontario, Canada. Dr. Sun received his Ph.D. in materials chemistry in 1999 from the University of Manchester, UK, which he followed up by working as a postdoctoral fellow at the University of British Columbia, Canada and as a Research Associate at L′Institut National de la Recherche Scientifique (INRS), Canada. His current research interests are focused on advanced materials for electrochemical energy storage and conversion, including electrocatalysis in fuel cells and electrodes in lithium-ion batteries and metal-air batteries.